Physics Letters A 431 (2022) 127991

Contents lists available at ScienceDirect

Physics Letters A

www.elsevier.com/locate/pla

Unpredictability in Hamiltonian systems with a hierarchical phase space

Matheus R. Sales [a], Michele Mugnaine [b], Ricardo L. Viana [b], Iberê L. Caldas [c], José D. Szezech Jr. [a,d,*]

[a] Postgraduate Program in Physics, State University of Ponta Grossa, 84030-900, Ponta Grossa, PR, Brazil
[b] Department of Physics, Federal University of Paraná, 80060-000, Curitiba, PR, Brazil
[c] Institute of Physics, University of São Paulo, 05508-900, São Paulo, SP, Brazil
[d] Department of Mathematics and Statistics, State University of Ponta Grossa, 84030-900, Ponta Grossa, PR, Brazil

ARTICLE INFO

Article history:
Received 22 October 2021
Received in revised form 1 February 2022
Accepted 4 February 2022
Available online 10 February 2022
Communicated by M. Perc

Keywords:
Uncertainty exponent
Stickiness
Conservative chaos
Weighted Birkhoff averages

ABSTRACT

One of the main consequences of the complex hierarchical structure of chaotic regions and stability islands in the phase space of a typical nonlinear Hamiltonian system is the phenomenon of stickiness. The chaotic orbits that approach an island are trapped in its neighborhood for arbitrarily long times, in which the orbits behave similarly as quasiperiodic orbits. In this paper, we characterize the boundary between chaos and regular motion in the phase space of the standard map for distinct parameter values. The orbits are distinguished between regular and chaotic employing a recently proposed method of weighted Birkhoff averages. We quantify the dimension of the boundaries of the islands using the uncertainty exponent. In our simulations, we show that the dimension of the island's boundary depends on the scale of the initial condition uncertainty and the level of the hierarchical structure. We also show that the trapping in the vicinity of the islands causes an obstruction in the predictability of the final state of an orbit. We present how this loss of predictability results in larger dimensions at the inner levels of the islands.

1. Introduction

The motion of a two-dimensional integrable Hamiltonian system takes place on periodic and quasiperiodic invariant tori. If a weak perturbation is added to such a system, the Kolmogorov-Arnold-Moser (KAM) theorem [1] states that sufficiently irrational tori survive the perturbation (KAM tori), while the rational ones are destroyed. In the vicinity of the original location of the destroyed rational tori, there exists a set of elliptic and hyperbolic points, as stated by the Poincaré-Birkhoff theorem [1], and chaotic motion appears in these regions. When the perturbation strength increases, the KAM tori are also destroyed and their remnants form an invariant Cantor-like set, also known as cantori [2,3].

Among the chaotic sea are found several islands of stability, making the phase space of a typical nonlinear Hamiltonian system neither integrable nor uniformly hyperbolic, where regular and chaotic behavior coexist. Due to the presence of the islands, the chaotic sea constitutes a fat fractal [4] and its exact boundary is difficult to determine due to the infinite hierarchical island-around-island structure embedded in it [5]. A direct consequence of this complex connection between regular and chaotic motion is the phenomenon known as stickiness [6–15]. The stickiness affects chaotic orbits that come close to an island. These orbits may spend an arbitrarily long but finite time in its neighborhood in which the orbit will present a similar behavior as a quasiperiodic orbit, until eventually it escapes. Before the orbit escapes to the chaotic sea, it remains trapped inside a region bounded by cantori [5,16] and once inside, the orbit may enter an inner cantorus, and so on to arbitrarily inner levels in the island-around-island hierarchy, and as a consequence the cantori act as partial barriers to the transport of chaotic orbits in phase space.

The importance of the phenomenon of stickiness was first noted by Contopoulos [6]. The stickiness has a large effect on global properties of the system, such as decay of correlations [7–9] and transport [10]. Altmann et al. [11,12] described that the stickiness for a two-dimensional Hamiltonian system with non-hierarchical borders between regular and chaotic regions is due to a family of marginally unstable periodic orbits. Cristadoro and

* Corresponding author at: Postgraduate Program in Physics, State University of Ponta Grossa, 84030-900, Ponta Grossa, PR, Brazil.
E-mail addresses: matheusrolim95@gmail.com (M.R. Sales), mmugnaine@gmail.com (M. Mugnaine), rlv640@gmail.com (R.L. Viana), ibere@if.usp.br (I.L. Caldas), jdsjunior@uepg.br (J.D. Szezech).

https://doi.org/10.1016/j.physleta.2022.127991
0375-9601/

Ketzmerick [13] described the generation of stickiness in two-dimensional Hamiltonian systems with a mixed phase space where they conjectured a universal power law decay of correlations. Contopoulos and Harsoula [14,15] demonstrated that in addition to the stickiness due to cantori that surround the islands of stability, there is another due to the unstable asymptotic curves of the unstable periodic orbits and they also related the escape time through a cantorus with the largest eigenvalue of the unstable periodic orbit, the size of the gaps of the cantorus and with the distance of the initial condition from the cantorus. Several methods have been proposed to identify stick orbits, such as the finite-time Lyapunov exponents [17,18], recurrence time statistics [11,12,19,20] and the finite-time rotation numbers [21,22].

The coexistence of regular and chaotic behavior on an arbitrarily small scale makes the task of distinguishing between these two regimes a non-trivial one. The standard test for chaos is the Lyapunov exponent method, where for two-dimensional Hamiltonian systems there are two exponents and they obey $\lambda_1 = -\lambda_2$. For periodic and quasiperiodic orbits, the Lyapunov exponent is zero while for the chaotic ones, $\lambda_1 > 0$. All stable, regular orbits have Lyapunov exponents equal to zero for infinite times. However, in the numerical simulations this limit is never reached and the Lyapunov exponent for different orbits shows distinct numerical convergence toward zero [23]. Although widely used, the Lyapunov exponent method has an extremely slow convergence rate of T^{-1}, where T is the orbit length [24]. Other methods have been proposed to efficiently distinguish between chaos and regularity, namely Fast Lyapunov Indicator, the 0–1 test, Mean Exponential Growth Factor of Nearby Orbits, among others. For a detailed discussion of these and other methods, see [25–27].

Recently, it was proposed a new method based on the ergodic partition theory for the calculation of observable time averages in phase space [28,29]. Even though this method also suffers from slow convergence due to their dependency on the use of Birkhoff averages, Das et al. were able to improve this method by combining it with their method of weighted Birkhoff averages [24,30–32]. In Ref. [24] the authors compare this new method with the 0–1 test and the Lyapunov exponents method and show that it has a better accuracy to distinguish between chaos and regularity and in the computation time.

In this paper, we aim to characterize the geometry of the boundary between chaotic and regular motion in the phase space of the standard map [33] for different levels in the hierarchical structure of islands and cantori. We use the weighted Birkhoff average method to test whether an orbit is regular or chaotic and we use the uncertainty fraction method [34–36] to obtain an effective fractal dimension [37,38] of the island's boundary. We find that the dimension depends on the scale of the initial condition uncertainty and on the position in phase space. We also point out that inner levels in the hierarchical structure show larger dimensions, due to the longer trapping time in the cantori.

This paper is organized as follows. In Section 2 we introduce the standard map and we briefly comment on some of its features when the non-linearity parameter is varied. In Section 3 we present the weighted Birkhoff method and in Section 4 we discuss the uncertainty fraction method. In Section 5 we obtain the effective dimension of the boundary of the islands for two values of the standard map non-linearity parameter and we show that we can associate an effective dimension with different scales of the initial condition uncertainty. We also show that the time a chaotic orbit spends in the vicinity of an island influences the effective dimension of the boundary. The last section contains our final remarks.

2. The standard map

To illustrate the effects of the complex hierarchical structure of chaotic regions and islands of stability, we use the paradigmatic standard map (or Chirikov-Taylor map) [33]. Besides its simplicity of being a two-dimensional Hamiltonian map, it has a very rich dynamics. The presence of embedded islands in the chaotic sea prevents the distribution of the finite Lyapunov exponent from having a single mode, in fact, it has a bimodal distribution in the presence of stickiness [17]. The trajectories cross the neighborhood of the islands through hyperbolic and non-hyperbolic regions that play an important role in the appearing of the stickiness phenomenon [39].

The dynamics of the standard map are given by the following equations

$$\begin{aligned} x_{t+1} &= x_t + y_{t+1} \mod 2\pi\,, \\ y_{t+1} &= y_t - k\sin x_t \mod 2\pi\,, \end{aligned} \tag{1}$$

where x_t and y_t are the two canonical dynamical variables, the position and the momentum, at discrete times $t = 0, 1, 2, \ldots, T$ and k is the non-linearity parameter which controls the degree of non-integrability in the system. The standard map is the discrete form of the canonical equations for the kicked rotor described by the Hamiltonian

$$H(x, y, t) = \frac{y^2}{2} - k\cos x \sum_{n=-\infty}^{\infty} \delta(t - n). \tag{2}$$

The dynamics takes place on a cylinder by taking $x \mod 2\pi$ or on a torus by taking x and $y \mod 2\pi$. In this paper, we will consider the latter.

If $k = 0$ the dynamics of the map is regular, the system is integrable, the momentum y_t is constant and every orbit lies on rotational invariant torus. As k increases, some of the irrational tori remain as invariant curves, as stated by the KAM theorem, and for appropriate initial conditions is possible to observe chaotic behavior. For the critical value $k = k_c \approx 0.971635$ [40] the last rotational torus is destroyed, leading to global stochasticity and one large chaotic orbit fills a significant portion of the phase space. For k not too large, several islands are still present in the chaotic sea and as k increases even further, the size of these islands decreases, until for sufficiently large values of k, the chaotic sea fills nearly the entire phase space [41]. In Fig. 1 is depicted this behavior for four different values of k.

3. The weighted Birkhoff average

In Refs. [24,30–32] the authors present a new method based on a weighted Birkhoff average for identifying chaotic orbits, island chains and rotational invariant tori. The Birkhoff average of a function $h(z)$ along the trajectory of a map $z_{t+1} = f^t(z_0)$ is

$$B(h)(z_0) = \frac{1}{T}\sum_{t=0}^{T-1} h \circ f^t(z_0). \tag{3}$$

The Birkhoff ergodic theorem [42] states that time averages of a function h along a trajectory $f^T(z_0)$, *i.e.*, $B(h)(z_0)$, converge to the space average

$$\frac{1}{T}\sum_{t=0}^{T-1} h \circ f^t(z_0) \to \int h\,\mathrm{d}\mu$$

as $T \to \infty$, where μ is an invariant probability measure. The Birkhoff average, however, does not have a fast convergence. For

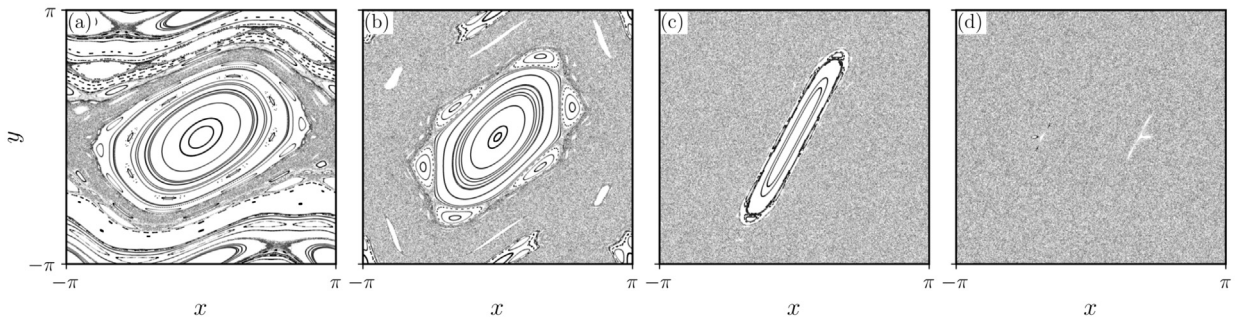

Fig. 1. Phase space of the standard map with 70 randomly chosen initial conditions for (a) $k = 0.9$, (b) $k = 1.5$, (c) $k = 4.0$, (d) $k = 6.908745$.

a quasiperiodic orbit, the convergence rate of (3) is of the order T^{-1}, because of the edge effects for the finite orbit segment. For the chaotic case the convergence rate is observed to be $T^{-1/2}$ [28].

The slow convergence is due to the lack of smoothness at the two ends of the orbit [24,31,32]. Therefore, instead of weighting the terms $h \circ f^t(z_0)$ in the average equally, they proposed very small weights to the terms when t is near 0 or T and defined the weighted Birkhoff average of a function $h(z)$ as

$$\mathrm{WB}(h)(z_0) = \sum_{t=0}^{T-1} w_{t,T} h \circ f^t(z_0), \tag{4}$$

where

$$w_{t,T} = \frac{1}{S} g\left(\frac{t}{T}\right), \; S = \sum_{t=0}^{T-1} g\left(\frac{t}{T}\right), \tag{5}$$

with

$$g(t) = \begin{cases} e^{-[t(1-t)]^{-1}} & \text{if } t \in (0,1), \\ 0 & \text{otherwise,} \end{cases}$$

being an exponential bump function that converges to zero with infinite smoothness at $t = 0$ and $t = 1$. Because of that, the weight function vanishes at the ends of the orbit segment, and thus preserves the smoothness of the original orbit [24,31,32].

It was shown in [32] that if $g(t)$ is a bump function infinitely differentiable, if the function h and the map f are also infinitely differentiable and $f^t(z_0)$ is a quasiperiodic orbit with Diophantine rotation vector, then (4) has a super-fast (super polynomial) convergence to the space average (see Theorems 1.1 and 3.1 in [32]), namely

$$\left| \mathrm{WB}(h)(z_0) - \int h \, \mathrm{d}\mu \right| \leq C_m T^{-m}.$$

For chaotic orbits, however, this method does not give any improvement in the convergence. Even though the constant C_m depends on the function h, the speed and the accuracy of the convergence to the phase space average are largely independent of the choice of h [30].

In order to classify an orbit as chaotic or regular, we compare the value of $\mathrm{WB}(h)(z_0)$ along the first T iterates with $\mathrm{WB}(h)(f^T(z_0))$ along the second T iterates. In the limit $T \to \infty$ these values should be equal [24] and we can measure the convergence rate by computing the number of zeros after the decimal point by defining

$$\mathrm{dig} = -\log_{10} \left| \mathrm{WB}(h)(z_0) - \mathrm{WB}(h)(f^T(z_0)) \right|. \tag{6}$$

If dig is large, the convergence is fast and the orbit is regular. If dig is small, the orbit is chaotic. However, we cannot compare

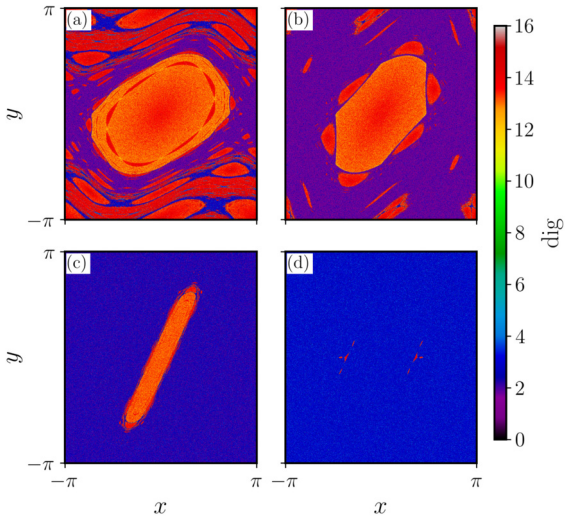

Fig. 2. (Color online.) The number of zeros dig after the decimal point for a 750×750 grid of uniformly distributed orbits of the standard map with (a) $k = 0.9$, (b) $k = 1.5$, (c) $k = 4.0$ and (d) $k = 6.908745$. WB_T was computed using $T = 10^6$ iterates and $h(z) = \cos x$. The values of dig are indicated in the color bar.

the small values of dig and say that an orbit with $\mathrm{dig} = 1$ is "more chaotic" than an orbit with $\mathrm{dig} = 3$, for example, because the weighted Birkhoff average method does not improve the convergence of such orbits. The total number of iterates needed to compute (6) is $2T$.

In Fig. 2 are shown the values of dig for a grid of 750×750 initial conditions for four different values of k of the standard map with $T = 10^6$ and $h(z) = \cos x$. A magnification of Figs. 2(c) and 2(d) are shown in Fig. 3 together with the histograms of dig. We see, as has been stated, that the smaller the parameter k, the greater the fraction of regular orbits. These orbits correspond to the distribution centered around $\mathrm{dig} \sim 14$ whilst the chaotic ones are centered around $\mathrm{dig} \sim 3.5$.

Although they occur less often, there are also orbits with intermediate values of dig. These are orbits trapped in the neighborhood of the island chains that experience weak chaos, also known as stickiness. Thus, we have to define a cutoff value for dig to distinguish between chaos and regularity. Meiss and Sander also addressed this problem in [43] to establish a cutoff value for dig. Based in our analysis of the histograms of dig, such the ones shown in Fig. 3, we choose the cutoff for $\mathrm{dig} = 11.25$ to detect the regular orbits. Because the number of orbits that have intermediate values of dig is small compared to regular and chaotic ones (see Figs. 3(b) and 3(d)), no significant changes will occur for small changes in the cutoff value and it will remain fixed for all our further analyses.

The specific choice of the function $h(z)$ is quite arbitrary, given that it satisfies the requirements of Theorems 1.1 and 3.1 in

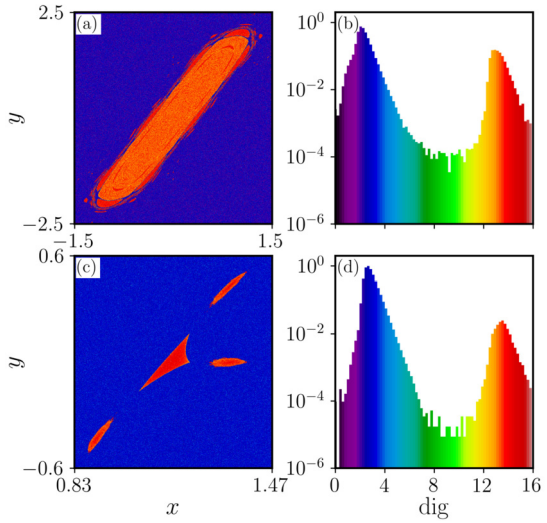

Fig. 3. (Color online.) (a) and (c) are magnifications of Figs. 2(c) and 2(d), respectively and (b) and (d) are their respective histograms. The color palette of the histograms matches the color bar of Fig. 2.

Ref. [32]. We use $h(z) = \cos x$, the same function used in Ref. [24] to compare the weighted Birkhoff average method with the Lyapunov exponents method and the 0–1 test. However, other functions also have been used. In Ref. [30] the authors used $h(z) = \sin(x + y)$ to demonstrate the method for the standard map and in Ref. [43], Meiss and Sander used the frequency map of a three-dimensional analog of the standard map as the function h.

4. Uncertainty fraction method

In this section we will discuss the uncertainty fraction method [34,35,44,45] used in the characterization of the boundary between chaotic and regular behavior in phase space.

To outline the method we consider a phase space region, as the one shown in Fig. 3(a), for example, and consider a large number of random initial conditions (x_0, y_0). For each initial condition (x_0, y_0) we evaluate dig by means of (6) with $T = 10^6$ and $h(z) = \cos x$. We then test whether dig is larger or not than the cutoff value. If so, we say the initial condition (x_0, y_0) is inside of an island, if not so, the pair lies on the chaotic sea. Each initial condition is then perturbed in the x direction by $\pm\epsilon$ to produce two new initial conditions $(x_0 \pm \epsilon, y_0)$. We evaluate dig for these new pairs of initial conditions and test again whether dig is larger or not than the cutoff value. If either of the two perturbed initial conditions has a different result, we say the original pair (x_0, y_0) is ϵ-uncertain. The uncertainty fraction $f(\epsilon)$ is the ratio between the number of ϵ-uncertain pairs and the total number of them.

We repeat these computations ten times with 5×10^4 pairs of initial conditions for each value of ϵ, which is varied from 10^{-2} to 10^{-8}. If the boundary is smooth, $f(\epsilon) \sim \epsilon$. This, however, is not the case for several nonlinear systems [46]. In these cases, the uncertainty fraction $f(\epsilon)$ is expected to scale with ϵ as a power law, namely

$$f(\epsilon) \sim \epsilon^{\alpha}, \tag{7}$$

with α being the uncertainty exponent [34–36].

It is possible to express the uncertainty exponent in terms of the capacity definition of dimension by letting D be the dimensionality of the phase space and $N(\delta)$ be the minimum number of D-dimensional boxes of length δ required to cover the boundary. Then, the capacity definition of dimension is

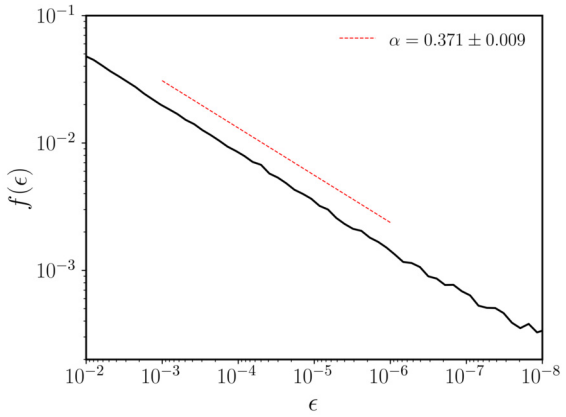

Fig. 4. (Color online.) Log-log plot of $f(\epsilon)$ versus ϵ for the region specified in Fig. 3(a) with $k = 4.0$. We observe a power law dependence with exponent $\alpha = 0.371 \pm 0.009$. Hence $d = 1.629 \pm 0.009$.

$$d = \lim_{\delta \to 0} \frac{\ln N(\delta)}{\ln 1/\delta}. \tag{8}$$

This definition simply points out that $N(\delta)$ scales as δ^{-d}, that is

$$N(\delta) \sim \delta^{-d}. \tag{9}$$

If we set $\delta \equiv \epsilon$, then the volume of the uncertain region on the phase space will be $N(\epsilon)\epsilon^D$, where ϵ^D is the volume of the boxes. With (9), the uncertain phase space volume is estimate to be $N(\epsilon)\epsilon^D \sim \epsilon^{D-d}$. Thus, the uncertainty exponent is [35]

$$\alpha = D - d. \tag{10}$$

In our case, the phase space has $D = 2$, such that $\alpha = 2 - d$. A smooth boundary, for which $d = 1$, has $\alpha = 1$, whereas a fractal boundary is characterized by $0 < \alpha < 1$ [34–36]. It is understood that fractal boundaries represent an obstruction to the predictability of the final state of nonlinear systems [34] and $f(\epsilon)$ can be considered as a measure of this unpredictability when the initial condition is given with an uncertainty of size ϵ. Therefore for fractal boundaries, in order to reduce the uncertainty of the final state, it may be necessary a considerable reduction in the initial condition uncertainty ϵ. A similar analysis of the dimension d was done in Ref. [44] for the parameter space of conservative systems.

5. Discussion

In Fig. 4 is shown the logarithmic plot of $f(\epsilon)$ versus ϵ for the standard map (1) with $k = 4.0$ for the same region in Fig. 3(a). The power law dependence is evident and we find that $\alpha = 0.371 \pm 0.009$. Thus, from (10), the dimension of the boundary is $d = 1.629 \pm 0.009$. Hence, if we want to improve by a factor of 2 the ability to predict whether the initial condition is regular or chaotic, it is necessary to increase the accuracy in the measurement of the initial condition by a factor of $2^{1/\alpha} = 2^{1/0.371} \approx 6.5$.

For $k = 4.0$ we see that the dimension of the boundary is constant over the specified range of the initial condition uncertainty ϵ. However, this is not always the case. Zaslavsky et al. showed in [47] that for a specific parameter of the standard map, namely $k = 6.908745$, there is a self-similar hierarchy of sub islands. We characterize the boundary of these sub islands and investigate the sensibility to the initial condition uncertainty ϵ. We demonstrate that in this case more than one dimension can be found, *i.e.*, we can associate different effective dimensions with different ranges of ϵ.

In order to determine the self-similar structure, we consider a 750×750 grid of initial conditions for each of the regions specified in Table 1 and count the time required for an orbit to escape

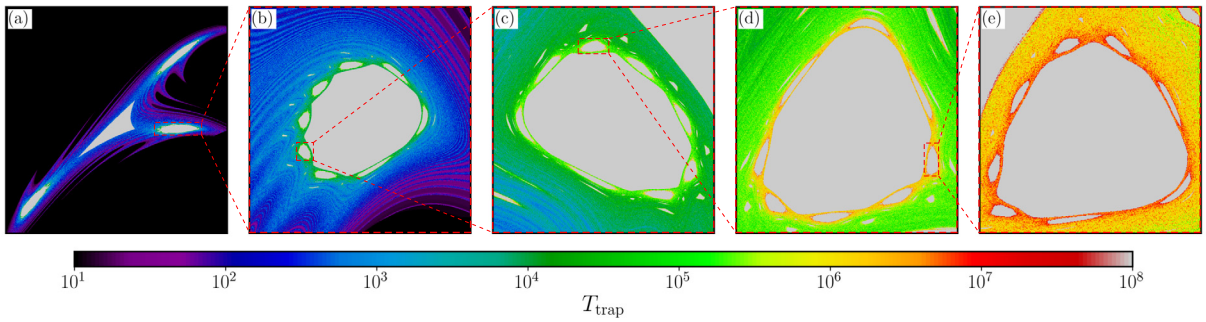

Fig. 5. (Color online.) Trapping time for a 750×750 grid of uniformly distributed initial conditions for the standard map with $k = 6.908745$. Figures (b)–(e) display magnifications around the indicated islands and the positions in phase space are specified in Table 1. The color bar is in logarithmic scale.

Table 1
Phase space regions shown in Fig. 5 given by $\{x, y \,|\, x_0 \geq x \geq x_1,\ y_0 \geq y \geq y_1\}$.

Fig. 5	x_0	x_1	y_0	y_1
(a)	0.83	1.47	−0.6	0.6
(b)	1.22	1.43	−0.05	0.05
(c)	1.2650	1.2794	−0.019	−0.009
(d)	1.2705	1.2725	−0.01103	−0.01046
(e)	1.27222	1.27234	−0.01089	−0.01079

the region with limits given by the first row of Table 1. The trapping time T_{trap} for the five regions in Table 1 is shown in Fig. 5. The regular orbits remain for all time inside the region (gray color) and the not-trapped chaotic orbits leave the box after a few iterations (black color). The intermediate values of T_{trap} correspond to trapped orbits and the magnifications in Figs. 5(b)–(e) show the stickiness structures and the self-similar hierarchy of sub islands. The sequence of self-similar islands generated by $k = 6.908745$ is 1-3-8-8-8, which means that the central island (1) is surrounded by three other islands (3) and each one of these islands are surrounded by eight islands (8) and so on. We will label this sequence as (p, q) where p represents the order of generation and q is the number of islands of the pth generation. For Fig. 5(c), for example, we have $(p, q) = (2, 8)$.

To investigate the sensibility to the initial condition uncertainty ϵ of the sub islands generated for $k = 6.908745$ we proceed in the same way as for $k = 4.0$. We compute the uncertainty fraction for the sequence of sub islands shown in Fig. 5 using 5×10^4 pairs of random initial conditions for each value of ϵ, which is varied from 10^{-2} to 10^{-8} for (a)–(c) and from 10^{-3} to 10^{-8} for (d) and (e). For each ϵ-uncertain pair $(x_{\text{unc}}, y_{\text{unc}})$ we also count the trapping time T_{trap}. We repeat these computations twenty-five times for (a) and (b) and ten times for (c)–(e). The logarithmic plots of $f(\epsilon)$ are shown in Fig. 6. The power law dependence is again evident, however now we can associate different exponents with different intervals of ϵ (except for Fig. 6(e)) and we evaluate the mean trapping time $\langle T_{\text{trap}} \rangle$ for each one of these intervals. The exponents, the dimensions and the mean trapping times $\langle T_{\text{esc}} \rangle$ are presented in Table 2.

Figs. 6(a)–(d) show a very similar behavior of $f(\epsilon)$. There are two decay rates in these cases, given by the exponents α_1 and α_2, where $\alpha_1 > \alpha_2$. In Fig. 6(e) for $10^{-3} \gtrapprox \epsilon \gtrapprox 10^{-5}$, we see that $f(\epsilon)$ does not obey a power law and this is due to the fact that the size of the island is comparable to this scale of ϵ and because of that, several false positive ϵ-uncertain pairs are found, causing the deviation from the power law. In fact, this argument is valid for all deviations from the power law behavior for large values of ϵ, as in Fig. 6(c) for $10^{-2} \gtrapprox \epsilon \gtrapprox 10^{-3}$, for example.

The existence of different exponents for different ranges of ϵ implies the existence of an effective fractal dimension [37,38] that depends on the scale of the initial condition uncertainty. In other words, at scale $\overline{\epsilon}_1$ the system behaves as if the fractal dimension is $d(\overline{\epsilon}_1) = d_1$, at scale $\overline{\epsilon}_2$, the system behaves as if $d(\overline{\epsilon}_2) = d_2$, etc. Thus, at different scales $\overline{\epsilon}_i$, the island boundary exhibits an effective fractal dimension $d(\overline{\epsilon}_i) = d_i$, which differs from the asymptotic value obtained when $\epsilon \to 0$. For the specified interval of ϵ, what we see is a smaller dimension for large values of ϵ, until it suddenly becomes larger for small ϵ.

We can relate the initial condition uncertainty ϵ to the resolution of a measuring device, and since fractal boundaries represent an obstruction to predictability, we can argue that if we want to improve the ability to predict whether the initial condition is regular or chaotic, we may need to increase the accuracy of the experiment by a larger factor depending on the resolution scale. For example, consider the island in Fig. 5(b). If the apparatus has an accuracy of 10^{-4} and we want to improve by a factor of 2 the ability to predict if the initial condition is regular or chaotic, we need to increase the accuracy by a factor of $2^{1/0.611} \approx 3.1$. On the other hand, if the apparatus has a resolution of 10^{-7}, the improvement in the accuracy has to be a factor of $2^{1/0.31} \approx 9.4$. Therefore, at realistic length scales, the uncertainty of the measurement is not determined by the asymptotic fractal dimension, but rather by the effective fractal dimension, as was previously reported in Ref. [38].

In [37,38,48] the authors showed that the dimension of the stable and unstable manifolds depends on the position in the phase space. We observe similar behavior for the dimension of the island's boundary. By applying the uncertainty fraction method for the region around the main island in Fig. 5(a), that is, the phase space region that contains only the island that is surrounded by the period-3 islands, we observe a dimension of $d = 1.013 \pm 0.009$ (not shown), which is clearly different from the dimension of the period-3 islands, shown in Fig. 6(b). Moreover, the order of generation of the island chains also influences the dimension of the boundary. We can see from Fig. 6 and from Table 2 that as we go deep into the self-similar structure, *i.e.*, increase p, the dimension for large values of ϵ, d_1, increases whereas the second dimension remains constant (within the uncertainty). Besides, there is a tendency of d_1 towards d_2 for increasing p, until $p = 4$ is reached and only one dimension is present for the specified interval of ϵ.

The order of generation of the island chains is directly related to the dimension of the boundary between regular and chaotic behavior due to the complex hierarchical structure of island chains and cantori. The farther inward we go into this structure, the longer the trajectories stay inside cantori, leading to very long trapping times, as shown in Fig. 5. These extremely long times impose difficulty in the prediction of the final state, hence the dimension of the inner levels is larger [37]. A similar result was found in [48] for the dynamics of a two-dimensional advection of a flow. Beyond that, we can see from Table 2 that the dimension and the mean trapping time for the second power law regime do not change significantly. We argue that this is so because at that scale of ϵ we are actually measuring an inner, finer level of the

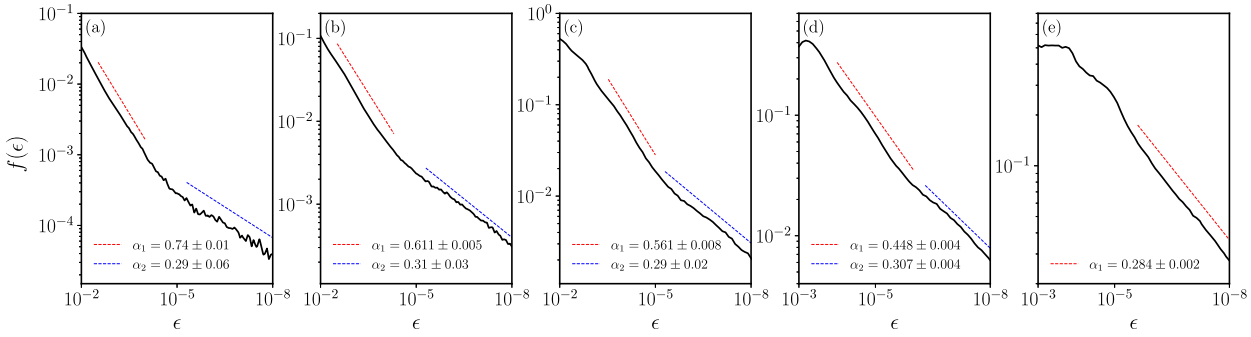

Fig. 6. (Color online.) Log-log plot of $f(\epsilon)$ versus ϵ for the regions shown in Fig. 5 and specified in Table 1 with $k = 6.908745$. The dashed lines indicate the slopes of $f(\epsilon)$.

Table 2
The uncertainty exponent α, the dimension d and the mean trapping time $\langle T_{\text{trap}} \rangle$ of the phase space regions shown in Fig. 5.

Fig. 5	α_1	d_1	$\langle T^{(1)}_{\text{trap}} \rangle$	α_2	d_2	$\langle T^{(2)}_{\text{trap}} \rangle$
(a)	0.74 ± 0.01	1.26 ± 0.01	2.8×10^4	0.29 ± 0.06	1.71 ± 0.06	1.2×10^6
(b)	0.611 ± 0.005	1.389 ± 0.005	1.5×10^5	0.31 ± 0.03	1.69 ± 0.03	1.6×10^6
(c)	0.561 ± 0.008	1.439 ± 0.008	5.3×10^5	0.29 ± 0.02	1.71 ± 0.02	1.6×10^6
(d)	0.448 ± 0.004	1.552 ± 0.004	1.9×10^6	0.307 ± 0.004	1.693 ± 0.004	2.7×10^6
(e)	0.284 ± 0.002	1.716 ± 0.002	7.3×10^6	–	–	–

self-similar hierarchy. Followed by that, we expect that decreasing even more the uncertainty in the initial conditions, more power law regimes with different exponents will be found. Even though our results were obtained for the standard map, we expect similar results for any typical nonlinear Hamiltonian system with a hierarchical phase space.

6. Conclusions

The stickiness phenomenon in nonlinear Hamiltonian systems is typically caused by the existence of a hierarchical island-around-island structure embedded in the chaotic sea, as in the standard map. We chose two values for the non-linearity parameter k to characterize the boundary between the chaotic sea and the islands, namely $k = 4.0$ and $k = 6.908745$.

In order to distinguish between the regular and chaotic behavior, we used the newly proposed method of weighted Birkhoff averages to compute time averages in phase space. Through the calculation of the quantity dig we are able to accurately test whether an initial condition (x_0, y_0) was inside of an island or in the chaotic sea. The characterization of the boundaries was made with the uncertainty fraction method, with which we obtained the dimension of the island's boundary for distinct values of k.

In our simulations, we verified that the boundary between the chaotic sea and the islands is indeed fractal, *i.e.*, the uncertainty exponent lies in the interval $(0, 1)$, hence a reduction in the uncertainty of the initial conditions will not result in a proportional reduction in the fraction $f(\epsilon)$ of ϵ-uncertainty pairs (x_0, y_0). We also showed that the uncertainty of the measurement is not determined by the asymptotic fractal dimension, but rather by the effective fractal dimension and this effective dimension depends on the interval of the initial condition uncertainty ϵ, implying that in order to obtain the desired reduction in $f(\epsilon)$, it is necessary to improve the accuracy in the measurement by a different factor, depending on the scale of the original resolution.

We showed that the dimension of the main island for $k = 6.908745$ is different from the dimension of the period-3 satellite islands. Furthermore, the dimension $d_1 \approx 1.2$, obtained in Fig. 6(a), is the dimension of the whole region depicted in Fig. 5(a), *i.e.*, the main island and the three satellite islands contribute to it, but individually they show distinct dimensions. In addition, the order of generation of the islands chains, or the level in the hierarchical structure, also affects the dimension. The farther inward we go into the structure, the larger is the dimension of the boundary, because the orbits that are trapped in the cantori take an arbitrarily long time to escape to the chaotic sea, and this leads to an obstruction in the predictability of the final state (whether it is chaotic or regular) of the orbit. Therefore, the uncertainty of orbits with long trapping times is greater due to the complexity of the island boundary, which imply a larger effective dimension [37].

At last, we showed that the dimension and the mean trapping time for the second power law regime are approximately constant. This reflects the fact that, for the parameter $k = 6.908745$ and the specified interval of ϵ, there are two length scales in the phase space. That is, the second power law regime is in fact measuring a finer level in the hierarchical structure. We used the standard map as a representative example, however, we claim that our results are still valid for a wide class of nonlinear Hamiltonian systems. One interesting point we plan to investigate in the future is the connection between the uncertainty fraction and the recurrence probability.

Data availability

The data that support the findings of this study are available from the corresponding author upon reasonable request.

CRediT authorship contribution statement

Matheus R. Sales: Writing – review & editing, Investigation, Methodology, Writing – original draft. **Michele Mugnaine:** Writing – review & editing, Writing – original draft, Methodology, Investigation. **Ricardo L. Viana:** Writing – review & editing, Writing – original draft, Methodology, Investigation. **Iberê L. Caldas:** Investigation, Methodology, Writing – original draft, Writing – review & editing. **José D. Szezech:** Writing – review & editing, Writing – original draft, Methodology, Investigation.

Declaration of competing interest

The authors declare that they have no known competing financial interests or personal relationships that could have appeared to influence the work reported in this paper.

Acknowledgements

We wish to acknowledge the support of the Araucária Foundation, the Coordination for the Improvement of Higher Education Personnel (CAPES), the National Council for Scientific and Technological Development (CNPq), under Grant Nos. 302665/2017-0, 407299/2018-1, 428388/2018-3, 311168/2020-5 and the São Paulo Research Foundation (FAPESP), under Grant No. 2018/03211-6. We would also like to thank the 105 Group Science (www.105groupscience.com) for fruitful discussions.

References

[1] A.J. Lichtenberg, M.A. Lieberman, Regular and Chaotic Dynamics, Applied Mathematical Sciences, vol. 38, Springer-Verlag, 1992.
[2] R.S. MacKay, J.D. Meiss, I.C. Percival, Stochasticity and transport in Hamiltonian systems, Phys. Rev. Lett. 52 (Feb. 1984) 697–700.
[3] R.S. MacKay, J.D. Meiss, I.C. Percival, Transport in Hamiltonian systems, Physica D 13 (1) (1984) 55–81.
[4] D.K. Umberger, J.D. Farmer, Fat fractals on the energy surface, Phys. Rev. Lett. 55 (Aug. 1985) 661–664.
[5] J.D. Meiss, E. Ott, Markov tree model of transport in area-preserving maps, Physica D 20 (2) (1986) 387–402.
[6] G. Contopoulos, Orbits in highly perturbed dynamical systems. iii. Nonperiodic orbits, Astron. J. 76 (Mar. 1971) 147.
[7] C.F.F. Karney, Long-time correlations in the stochastic regime, Physica D 8 (3) (1983) 360–380.
[8] J.D. Meiss, J.R. Cary, C. Grebogi, J.D. Crawford, A.N. Kaufman, H.D. Abarbanel, Correlations of periodic, area-preserving maps, Physica D 6 (3) (1983) 375–384.
[9] B.V. Chirikov, D. Shepelyansky, Correlation properties of dynamical chaos in Hamiltonian systems, Physica D 13 (3) (1984) 395–400.
[10] G.M. Zaslavsky, Chaos, fractional kinetics, and anomalous transport, Phys. Rep. 371 (6) (2002) 461–580.
[11] E.G. Altmann, A.E. Motter, H. Kantz, Stickiness in mushroom billiards, Chaos 15 (3) (2005) 033105.
[12] E.G. Altmann, A.E. Motter, H. Kantz, Stickiness in Hamiltonian systems: from sharply divided to hierarchical phase space, Phys. Rev. E 73 (Feb. 2006) 026207.
[13] G. Cristadoro, R. Ketzmerick, Universality of algebraic decays in Hamiltonian systems, Phys. Rev. Lett. 100 (May 2008) 184101.
[14] G. Contopoulos, M. Harsoula, Stickiness in chaos, Int. J. Bifurc. Chaos 18 (10) (2008) 2929–2949.
[15] G. Contopoulos, M. Harsoula, Stickiness effects in conservative systems, Int. J. Bifurc. Chaos 20 (07) (2010) 2005–2043.
[16] C. Efthymiopoulos, G. Contopoulos, N. Voglis, R. Dvorak, Stickiness and Cantori, J. Phys. A, Math. Gen. 30 (Dec. 1997) 8167–8186.
[17] J.D. Szezech, S.R. Lopes, R.L. Viana, Finite-time Lyapunov spectrum for chaotic orbits of non-integrable Hamiltonian systems, Phys. Lett. A 335 (5) (2005) 394–401.
[18] R.M. da Silva, C. Manchein, M.W. Beims, E.G. Altmann, Characterizing weak chaos using time series of Lyapunov exponents, Phys. Rev. E 91 (Jun. 2015) 062907.
[19] C.V. Abud, R.E. de Carvalho, Multifractality, stickiness, and recurrence-time statistics, Phys. Rev. E 88 (Oct. 2013) 042922.
[20] Č. Lozej, Stickiness in generic low-dimensional Hamiltonian systems: a recurrence-time statistics approach, Phys. Rev. E 101 (May 2020) 052204.
[21] J.D. Szezech, A.B. Schelin, I.L. Caldas, S.R. Lopes, P.J. Morrison, R.L. Viana, Finite-time rotation number: a fast indicator for chaotic dynamical structures, Phys. Lett. A 377 (6) (2013) 452–456.
[22] M.S. Santos, M. Mugnaine, J.D. Szezech, A.M. Batista, I.L. Caldas, R.L. Viana, Using rotation number to detect sticky orbits in Hamiltonian systems, Chaos 29 (4) (2019) 043125.
[23] C. Manchein, M.W. Beims, Conservative generalized bifurcation diagrams, Phys. Lett. A 377 (10) (2013) 789–793.
[24] E. Sander, J.D. Meiss, Birkhoff averages and rotational invariant circles for area-preserving maps, Physica D 411 (2020) 132569.
[25] G.A. Gottwald, I. Melbourne, On the implementation of the 0–1 test for chaos, SIAM J. Appl. Dyn. Syst. 8 (1) (2009) 129–145.
[26] C. Froeschlé, E. Lega, R. Gonczi, Fast Lyapunov indicators. Application to asteroidal motion, Celest. Mech. Dyn. Astron. 67 (1) (1997) 41–62.
[27] C.H. Skokos, G.A. Gottwald, J. Laskar, Chaos Detection and Predictability, Lecture Notes in Physics, vol. 915, Springer-Verlag, 2016.
[28] Z. Levnajić, I. Mezić, Ergodic theory and visualization. i. Mesochronic plots for visualization of ergodic partition and invariant sets, Chaos 20 (3) (2010) 033114.
[29] Z. Levnajić, I. Mezić, Ergodic theory and visualization. ii. Fourier mesochronic plots visualize (quasi)periodic sets, Chaos 25 (5) (2015) 053105.
[30] S. Das, C.B. Dock, Y. Saiki, M. Salgado-Flores, E. Sander, J. Wu, J.A. Yorke, Measuring quasiperiodicity, Europhys. Lett. 114 (May 2016) 40005.
[31] S. Das, Y. Saiki, E. Sander, J.A. Yorke, Quantitative quasiperiodicity, Nonlinearity 30 (Oct. 2017) 4111–4140.
[32] S. Das, J.A. Yorke, Super convergence of ergodic averages for quasiperiodic orbits, Nonlinearity 31 (Jan. 2018) 491–501.
[33] B.V. Chirikov, A universal instability of many-dimensional oscillator systems, Phys. Rep. 52 (5) (1979) 263–379.
[34] C. Grebogi, S.W. McDonald, E. Ott, J.A. Yorke, Final state sensitivity: an obstruction to predictability, Phys. Lett. A 99 (9) (1983) 415–418.
[35] S.W. McDonald, C. Grebogi, E. Ott, J.A. Yorke, Fractal basin boundaries, Physica D 17 (2) (1985) 125–153.
[36] C. Gregobi, E. Ott, J.A. Yorke, Chaos, strange attractors, and fractal basin boundaries in nonlinear dynamics, Science 238 (4827) (1987) 632–638.
[37] A.P.S. de Moura, C. Grebogi, Reactions in flows with nonhyperbolic dynamics, Phys. Rev. E 70 (Sep. 2004) 036216.
[38] A.E. Motter, A.P.S. de Moura, C. Grebogi, H. Kantz, Effective dynamics in Hamiltonian systems with mixed phase space, Phys. Rev. E 71 (Mar. 2005) 036215.
[39] T.S. Krüger, P.P. Galuzio, T.d.L. Prado, R.L. Viana, J.D. Szezech, S.R. Lopes, Mechanism for stickiness suppression during extreme events in Hamiltonian systems, Phys. Rev. E 91 (Jun. 2015) 062903.
[40] J.M. Greene, A method for determining a stochastic transition, J. Math. Phys. 20 (6) (1979) 1183–1201.
[41] R. Venegeroles, Leading Pollicott-Ruelle resonances for chaotic area-preserving maps, Phys. Rev. E 77 (Feb. 2008) 027201.
[42] I.P. Cornfeld, S.V. Fomin, Y.G. Sinai, Ergodic Theory, vol. 245, Springer-Verlag, 1982.
[43] J.D. Meiss, E. Sander, Birkhoff averages and the breakdown of invariant tori in volume-preserving maps, Physica D 428 (2021) 133048.
[44] A.C. Mathias, M. Mugnaine, M.S. Santos, J.D. Szezech, I.L. Caldas, R.L. Viana, Fractal structures in the parameter space of nontwist area-preserving maps, Phys. Rev. E 100 (Nov. 2019) 052207.
[45] M. Mugnaine, A.C. Mathias, M.S. Santos, A.M. Batista, J.D. Szezech, R.L. Viana, Dynamical characterization of transport barriers in nontwist Hamiltonian systems, Phys. Rev. E 97 (Jan. 2018) 012214.
[46] J. Aguirre, R.L. Viana, M.A.F. Sanjuán, Fractal structures in nonlinear dynamics, Rev. Mod. Phys. 81 (Mar. 2009) 333–386.
[47] G.M. Zaslavsky, M. Edelman, B.A. Niyazov, Self-similarity, renormalization, and phase space nonuniformity of Hamiltonian chaotic dynamics, Chaos 7 (1) (1997) 159–181.
[48] H. Aref, J.R. Blake, M. Budišić, S.S.S. Cardoso, J.H.E. Cartwright, H.J.H. Clercx, K. El Omari, U. Feudel, R. Golestanian, E. Gouillart, G.F. van Heijst, T.S. Krasnopolskaya, Y. Le Guer, R.S. MacKay, V.V. Meleshko, G. Metcalfe, I. Mezić, A.P.S. de Moura, O. Piro, M.F.M. Speetjens, R. Sturman, J.-L. Thiffeault, I. Tuval, Frontiers of chaotic advection, Rev. Mod. Phys. 89 (Jun. 2017) 025007.